J Mater Sci (2021) 56:15040–15060

Chemical routes to materials

Self-lubricating triboactive (Cr,Al)N+Mo:S coatings for fluid-free applications

K. Bobzin[1], T. Brögelmann[1], C. Kalscheuer[1], and M. Thiex[1,*]

[1] *Surface Engineering Institute (IOT), RWTH Aachen University, Kackertstr. 15, 52072 Aachen, Germany*

Received: 4 March 2021
Accepted: 9 June 2021
Published online: 1 July 2021

ABSTRACT

Within this study, self-lubricating and triboactive (Cr,Al)N+Mo:S coatings were developed and investigated for the deposition on components in a low-temperature physical vapor deposition (PVD) hybrid process. Therefore, direct current magnetron sputtering (dcMS) and high power pulse magnetron sputtering (HPPMS) PVD were combined by using an industrial coating machine. Hereby, it was possible to deposit dense and smooth triboactive, self-lubricating nitride coatings with different chemical compositions and architectures on 16MnCr5E samples. Two coating architectures, a matrix monolayer and a graded coating structure, were developed to evaluate the effect on the tribological behavior. The morphology and coating thickness were analyzed by means of scanning electron microscopy (SEM). Furthermore, the indentation hardness and modulus of indentation as well as the compound adhesion between substrate materials and coating were analyzed. Tribological analyses of (Cr,Al)N+Mo:S-coated and uncoated samples were conducted under fluid-free friction regime at room temperature $T=(20\pm3)$ °C, a velocity $v=0.1$ m/s and a distance $s=1000$ m by varying the Hertzian contact pressure from 400 MPa$\leq p_H\leq$ 1300 MPa against steel counterparts, 100Cr6, in a pin-on-disk (PoD) tribometer. The graded coating architecture of (Cr,Al)N+Mo:S enabled a significant wear and friction reduction. Furthermore, Raman analyses prove the formation of solid lubrication tribofilm containing MoS_2, MoO_3 MoO_2 and Mo_xO_y at the toplayer of a graded (Cr,Al)N+Mo:S coating, which are responsible for the improved tribological behavior.

Handling Editor: Yaroslava Yingling.

Address correspondence to E-mail: thiex@iot.rwth-aachen.de

https://doi.org/10.1007/s10853-021-06255-9

Introduction

Today, gearboxes are conventionally lubricated with greases or oils. However, mineral oil or synthetic oil-based lubricants are often not applicable in medical technology, food technology, production under vacuum processes technology and aerospace applications due to extreme ambient conditions. Moreover, lubrication requires a high level of machine component design due to the use of complex sealing systems, e.g., in gearboxes. In the absence of conventional lubricants, friction increases, which leads to a high thermal load and thus to rising of mechanical stresses and accelerated failure of components [1, 2]. Spur gears that are exposed to high mechanical loads without conventional grease or oil lubrication show considerable damage after a short operating time due to the enormous heat input caused by friction [3, 4]. Typical damage patterns on gears are scuffing and hot running. A friction reduction can be achieved by using solid lubricants like graphite or molybdenum disulfide (MoS_2). However, these solid lubricants are rarely developed for high mechanical loads.

A possible solution could be the fluid-free lubrication with solid lubricants such as transition metal dichalcogenides (TMD) like molybdenum disulfide (MoS_2) which are widely used in the industry. The crystallographic hexagonal structure of MoS_2 is bonded by weak van der Waals forces between the planes. Here, a sliding on planes against each other can be initiated through low shear stresses and leading to a friction reduction in tribological systems. A possible application of MoS_2 coatings on components can be conducted by means of MoS_x physical vapor deposition. Despite the friction reduction in tribological contacts, high wear rates can lead to fast coating failures depending on the structure and chemical composition under high loads [5]. For this reason, different coating architecture concepts to improve the tribological behavior of Mo- and S-containing coatings are pursued in the literature. One coating concept follows the approach of adding different metals Al, Cr, Ti to a MoS_2 monolayer [6–8]. Furthermore, hard soft combinations with a hard nitride-based coating and a soft MoS_2 toplayer are also a possible solution to improve the tribological behavior of MoS_2 containing PVD coatings [8]. However, the disadvantage of these coating architecture concepts is that the low wear resistant solid lubricant MoS_2 toplayer also forms the lubricant depot at the same time, while the hard support layer below only serves as wear protection.

An alternative approach pursues the incorporation of disulfide solid lubricants into a hard coating matrix, which serves to increase the wear resistance and as a depot for solid lubricant storage. The nitride hard coatings CrN, TiN and (Cr,Al)N are well known as wear protection coatings on cutting tools in industrial applications [9–12]. In general, the use of nitride-based coatings in dry-running tribological contacts leads to a wear reduction for the coated contact partner, whereby wear rises for uncoated counterparts. Hereby also the friction in the tribological contacts with uncoated components increases [13]. Investigations of TiN, CrN, and (Cr,Al)N as a matrix material for the incorporation of Mo and S were carried out by [14–16]. Here, the negative effects regarding wear could be reduced and a friction reduction could be achieved. The chemical analyses on the modification elements Mo and S in the (Cr,Al)N and TiN layer systems have shown that MoS_2 is not necessarily stoichiometrically present in the matrix [14, 16].

Within the scope of this study, the goal was to investigate the effect of two different coating architectures on friction reduction by the solid lubricant MoS_2 and increased wear resistance through the use of (Cr,Al)N. For this purpose, the two coating architecture concepts (i) matrix and (ii) graded (Cr,Al)N coating with a nitride-based toplayer and embedded Mo and S were developed and analyzed. The intended application of the developed coatings is highly loaded spur gears running under dry conditions. Therefore, the case-hardened steel 16MnCr5E, which is conventionally used for gears, was chosen as substrate material, which requires a low-temperature coating PVD process due to the low annealing temperature $T \leq 300$ °C. This can be achieved by means of a hybrid process of direct current magnetron sputtering (dcMS) and high power pulse magnetron sputtering (HPPMS) coating process [17]. Chemical analysis, analysis of the microstructure, indentation hardness and modulus of indentation enable a basic understanding of the coatings and there architecture. In addition, tribological analyses at different Hertzian contact pressure from 400 MPa $\leq p_H \leq$ 1300 MPa under fluid-free friction regime at room temperature $T = (20 \pm 3)$ °C were conducted. After tribological testing,

Raman analyses were conducted to prove the supply mechanism of the graded coating and transfer mechanism to the 100Cr6 counterpart. Particularly in the field of highly loaded tribological contacts there is substantial need for research regarding the design of dry-running tribological systems and their supply mechanisms of solid lubricants.

Experimental details

Coating deposition

The molybdenum Mo- and sulfur S-containing (Cr,Al)N+Mo:S coatings were deposited in an industrial scale coating machine CC800/9 HPPMS, CemeCon AG, Würselen, Germany, by developing a low-temperature coating process $T \leq 300$ °C. The coating unit was equipped with four dcMS cathodes and two HPPMS cathodes. Both technologies were combined in a dcMS/HPPMS process, due to the beneficial advantages of high ionization regarding improved mechanical properties, low roughness, dense microstructure, coating of complex geometries and enhanced compound adhesion between substrate and coating [18–21]. The arrangement of the cathodes and the layout of the deposition chamber are depicted in Fig. 1a.

For the deposition of the (Cr,Al)N+Mo:S coatings, Al plugged Cr targets (purity Cr 99.95%, purity Al 99.5%), a Cr plugged Al target (purity Al 99.5%, purity Cr 99.5%), and a MoS_2 target (purity 99.5%) were used. The notations CrAl20 and AlCr30 refer to a Cr target with 20 Al plugs or an Al target with 30 Cr plugs respectively. The dimensions of the targets were 500 mm × 88 mm, and the diameter of the Al or Cr plugs was approximately Ø ≈ 15 mm, Fig. 1b. The process parameters for the deposition of the reference coating (Cr,Al)N are presented in [22]. In this study, two different coating architectures, a monolayer matrix (M) and a graded (G) (Cr,Al)N+Mo:S structure, Fig. 2, were developed and compared with the reference coating (Cr,Al)N. The idea of the monolayer matrix coating was to produce a coating with a constant depot of embedded Mo and S depots from the intermediate layer to the toplayer. This should enable the in situ formation of the solid lubricant MoS_2 during the tribological contact, Fig. 2a.

An alternative coating concept is described by the graded coating architecture, whereby besides the changes of the chemistry at the monolayer matrix coating, a differing interlayer design and chemical composition of the toplayer are developed, Fig. 2b. Hereby, the ratio of Mo and S is increased toward the toplayer but still embedded in a nitride matrix. Therefore, three different coatings of each architecture were deposited and analyzed.

The coatings were deposited on case-hardened 16MnCr5E steel samples (Ø=25 mm, H=8 mm) polished to a roughness Ra=0.02 µm. The case-hardened steel 16MnCr5E had a surface hardness of H=(60±2) HRC with a case hardening depth d_c=1 mm, to ensure a sufficient load carrying capacity for the (Cr,Al)N+Mo:S coatings. The development of self-lubricating (Cr,Al)N+Mo:S coatings by means of dcMS/HPPMS for components was based on process

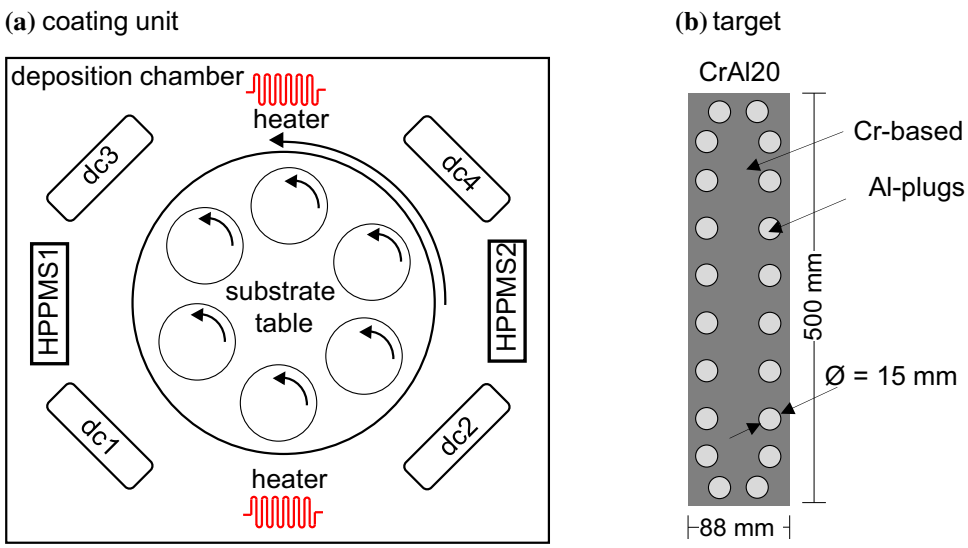

Figure 1 Schematic representation of the industrial coating unit CC800/9 HPPMS.

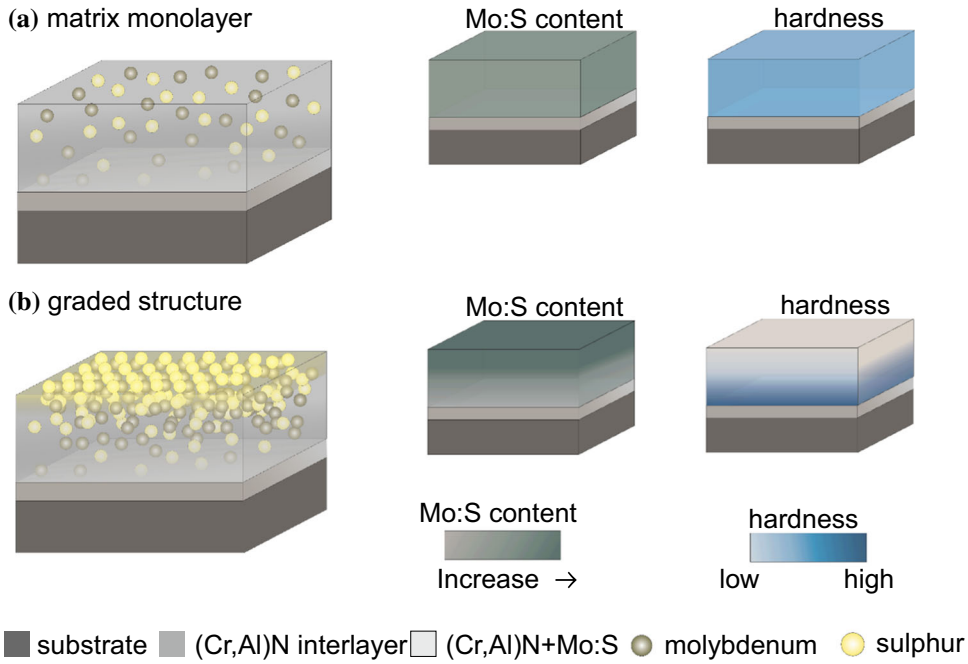

Figure 2 Schematic representation matrix monolayer and graded coating architecture.

parameters of low-temperature coating process of (Cr,Al)N published in [22] and the target configuration of (Cr,Al)N+Mo:S coating for tools given in [14]. Moreover, the in situ temperature measurement system developed at IOT presented in [23] for determining the substrate temperature depending on cathode powers during the coating process was used to avoid an excessive overshooting of the annealing temperature $T \leq 200$ °C of 16MnCr5E. The target configurations for the deposition processes of the coatings are presented in Table 1. In order to increase the Mo:S content at the toplayer for M3, two MoS_2 targets were chosen.

This concept was adopted for the graded coatings. Exchanging a CrAl20 with an AlCr30 target could lead to changes of the coating structure, which could be beneficial for the tribological behavior. The process parameters and bold changes of the developed matrix M1–M3 and graded G1–G3 (Cr,Al)N+Mo:S coatings for the deposition of interlayer and toplayer are shown in Tables 2 and 3.

Coating and compound analysis

The coating thicknesses and morphology were investigated by scanning electron microscopy (SEM) analyses, Oxford Link ISIS, Oxford Instruments plc, UK, at the Central Facility for Electron Microscopy (GfE), RWTH Aachen University, Aachen, Germany. The chemical composition over the coating thickness was analyzed by means of X-ray microanalysis (EPMA) on the basis of a calotte. The calotte was generated by rotating a hardened steel ball combined with diamond suspension for $t = 60$ s on the coating. Phase analyses of the developed (Cr,Al)N+Mo:S coatings were conducted by X-ray diffraction (XRD) measurements using grazing incidence diffraction (GID), XRD 3003, GE Energy Germany GmbH,

Table 1 Target configuration for the deposition of matrix and graded (CrAl)N+Mo:S coatings

Coating process	HPPMS1	HPPMS2	dc1	dc2	dc3	dc4
M1	CrAl20	CrAl20	CrAl20	MoS_2	CrAl20	CrAl20
M2	CrAl20	CrAl20	CrAl20	MoS_2	CrAl20	CrAl20
M3	CrAl20	CrAl20	CrAl20	**MoS_2**	**MoS_2**	CrAl20
G1	CrAl20	CrAl20	CrAl20	MoS_2	MoS_2	CrAl20
G2	CrAl20	CrAl20	**AlCr30**	MoS_2	MoS_2	CrAl20
G3	CrAl20	CrAl20	**AlCr30**	MoS_2	MoS_2	CrAl20
(Cr,Al)N	CrAl20	CrAl20	–	–	–	CrAl20

Table 2 Process parameters of (Cr,Al)N+Mo:S matrix monolayer coatings

Process phase	Process parameter [unit]	M1	M2	M3
Interlayer	Pulsed bias voltage, $U_{B,HPPMS}$ [V]	−100	−100	**−150**
	Nitrogen pressure controlled, p_{N2} [mPa]	660	**560**	560
	Argon gas flow, Q_{Ar} [sccm]	200	200	200
	Cathode power, P_{dc}(CrAl20) [W]	500	500	500
	Cathode power, P_{dc}(MoS_2) [W]	500	500	500
	Ramped cathode power, P_{HPPMS} [W]	500–4500	**500–5000**	500–5000
	Pulse-on-time, t [µs]	40	40	40
	Pulse frequency, f [Hz]	500	500	500
	Process time, t_p [s]	1425	1425	1425
Toplayer	Nitrogen pressure controlled, p_{N2} [mPa]	710	710	**550**
	Argon gas flow, Q_{Ar} [sccm]	200	200	200
	Ramped cathode power, P_{dc}(CrAl20) [W]	500–800	500–800	500–800
	Ramped cathode power, P_{dc}(MoS_2) [W]	500–800	500–800	500–800
	Cathode power, P_{HPPMS} [W]	2500	**4500**	4500
	Process time, t_p [s]	3600	3600	3600

Table 3 Process parameters of graded (Cr,Al)N+Mo:S coatings

Process phase	Process parameter [unit]	G1	G2	G3
Interlayer	Pulsed bias voltage, $U_{B,HPPMS}$ [V]	−150–(−75)	−150–(−75)	−150–(−75)
	Nitrogen pressure controlled, p_{N2} [mPa]	500	500	500
	Argon gas flow, Q(Ar) [sccm]	200	200	200
	Ramped cathode power, P_{dc}(CrAl20, AlCr30) [W]	800–0	800–0	800–0
	Ramped cathode power, P_{dc}(MoS_2) [W]	800–3800	800–3800	800–3800
	Ramped cathode power, P_{HPPMS} [W]	4500–0	4500–0	**4500–2000**
	Pulse-on-time, t [µs]	40	40	40
	Pulse frequency, f [Hz]	500	500	500
	Process time, t_p [s]	6845	6845	6845
Toplayer	Nitrogen gas flow, $Q(N_2)$ [sccm]	75–0	75–0	**150–100**
	Argon pressure controlled, p_{Ar} [mPa]	500	500	**600**
	Cathode power, P_{dc} (MoS_2) [W]	3800	3800	3800
	Cathode power, P_{HPPMS} [W]	–	–	**2000**
	Process time, t_p [s]	920	920	920

Ratingen, Germany. The measurements were carried out by means of Cu-Kα radiation, wavelength λ= 0.1540598 nm, U=40 kV, I=40 mA, diffraction angle 2θ=10°– 80°, incidence angle ω=2°, step width s= 0.05°, step time t=10 s. A nanoindenter of type TI 950 TriboIndenter, Bruker Corporation, Billerica, Massachusetts, USA, with a Berkovich indenter was applied for the determination of the indentation hardness H_{IT} and modulus of indentation E_{IT}. The samples were as-deposited, and the used constant indentation force was F=10 mN. In order to determine H_{IT} and E_{IT}, x=40 individual measurements were conducted and subsequently averages were calculated. The penetration depth was kept below 10% of the thickness of the toplayer. Calculations of the modulus of indentation are based on Oliver and Pharr's equations [24]. A constant Poisson's ratio of υ =0.25 was assumed for the coatings. The scratch tester Gesellschaft für Fertigungstechnik und Entwicklung Schmalkalden e.V. (GFE), Schmalkalden, Germany, was used for the compound adhesion analysis between coating and case-hardened 16MnCr5E. The scratch tests were conducted with a Rockwell C diamond at different constant forces in the area of 10 N≤F_N≤80 N in steps of F_N=10 N. Every scratch was generated with a length of x_s=

4 mm and a feed speed v_f=10 mm/min. The load was applied during the first x_s=0.2 mm of the total scratch length. In accordance to DIN EN ISO 20502 [25] the compound adhesion between coating and substrate was evaluated by scratch tests and confocal laser scanning microscopy (CLSM), VK-X210, Keyence, Neu-Isenburg, Germany. The resulting critical loads $Lc_{1\text{-}3}$ had been measured and used to assess adhesion strength for a specific reference compound coating/substrate.

Tribological analysis

The samples were tested under pure sliding conditions in a PoD tribometer, CSM Instruments, Peseux, Switzerland. Tribological tests were conducted at fluid-free friction regime in a steel/steel and coating/steel contact at different initial Hertzian pressure p_H= 400 MPa, p_H=600 MPa, p_H=800 MPa and p_H= 1300 MPa calculated based on basic part and counterpart properties. Therefore, the normal force was adjusted to F_N=0.5 N for p_H=400 MPa and F_N=2 N for p_H=600 MPa by using an uncoated Ø=10 mm diameter 100Cr6 ball. With regard to the higher initial Hertzian loads, uncoated 100Cr6 balls with a diameter of Ø=6 mm were chosen at a normal force of F_N =2 N for p_H=800 MPa and F_N=8 N for p_H=1300 MPa. It has to be stated that all considered Hertzian pressures can be regarded as an initial value, which will change during the tribological contact due to wear of basic part and counterpart. The chosen initial Hertzian pressure enables a mapping of different applications like in equipment in food or pharmaceutical industries and optical devices. Gears are conventionally running under sliding and rolling conditions during the tribological contact. However, the PoD testing under pure sliding conditions causes high load inputs to the compound of coating and 16MnCr5E, so that an assessment can be obtained with regard to the application of the developed coatings on gears. The parameters relative velocity v_{rel}=0.1 m/s, radius r=2.5 mm, distance s=1000 m room temperature $T=RT \triangleq T=(20\pm3)$ °C and relative humidity $\varphi \approx (45\pm5)$ % were kept constant. In addition, a repetition of each tribological test was carried out. The average coefficients of friction (CoF) were evaluated for the final s=500 m running distance. Topography and wear analysis of the wear tracks on the basic parts and wear areas on the counterparts were conducted on one of the two samples after tribological testing by means of CLSM.

Chemical analysis of tribologically tested samples by Raman spectroscopy

For chemical analysis after tribological testing, the Raman spectrometer, Renishaw InVia Reflex, Renishaw GmbH, Pliezhausen, Germany, with a λ= 532 nm laser with a spot size of $d \approx 1$ µm and a diffraction grating $g(\lambda=532\text{ nm})=1800$ 1/mm, was used. Here, a graded (Cr,Al)N+Mo:S-coated basic part and a 100Cr6 counterpart were exemplarily analyzed regarding the tribofilm formation. The measuring parameters were adjusted to the different samples. The laser was calibrated before the measurement by using a silicon reference sample.

Results and discussion

Temperature measurement of coating process parameters

The in situ temperature measurement system proves that high HPPMS cathode power up to P=5000 W has a neglectable effect on the substrate temperature of the 16MnCr5E samples. In contrast thereto, the addition of four parallel running dc cathodes to the HPPMS cathodes limits the power of the dc cathodes to P=800–1000 W. These results enabled the development of a low-temperature coating process for the deposition of the different coating architectures (i) matrix monolayer and (ii) graded. In Fig. 3, the measured substrate temperature during the coating process of G3 divided in the four main sections is shown.

It can be observed that during the coating deposition the annealing temperature of 16MnCr5E 150 °C≤ T≤200 °C is exceeded to T=264 °C. However, the effect on the loss of hardness is negligible. The data sheet in [26] shows that the hardness loss at T=300 °C is around 1 HRC≤H≤3HRC. These values are within the range of deviation for the case hardening process of H=(60±2) HRC. Also Rockwell indentation tests of steel samples after the deposition process did not show any changes of the hardness. Nevertheless, the process was developed close to the limits of the acceptable temperature load of 16MnCr5E during the coating deposition.

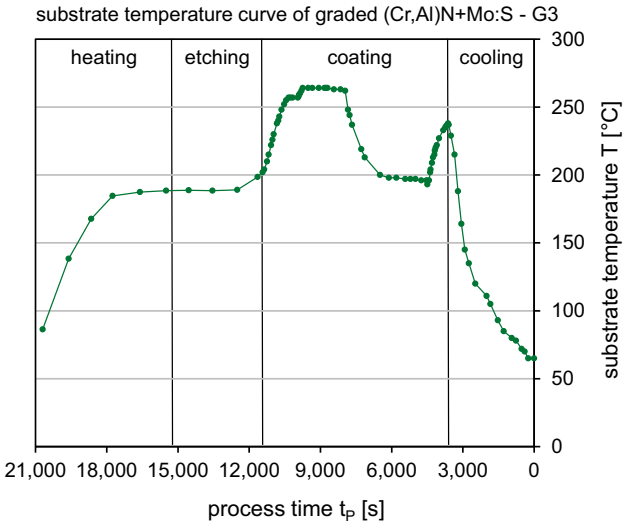

Figure 3 Substrate temperature curve of graded (Cr,Al)N+Mo:S coating process.

Matrix coating development

In a first step, self-lubricating (Cr,Al)N+Mo:S monolayer matrix coatings were developed. Figure 4 shows the cross-sectional micrographs of the three developed (Cr,Al)N+Mo:S monolayer matrix coatings, as well as the reference coating (Cr,Al)N.

It can be observed that the matrix coatings and the (Cr,Al)N coating possess a dense and fine columnar structure. Due to changes of bias voltage U_B, HPPMS cathode power P_{HPPMS} and nitrogen pressure p_{N2} in the coating processes M1–M3 highlighted in Table 2, the coating thicknesses are ranging between 1.3 µm ≤ t ≤ 2.1 µm. In addition, a smooth surface structure with only little defects at the toplayer can be found for all coatings, which can be explained by the use of the HPPMS technology. The depth-resolved chemical compositions of the coatings by means of EPMA are shown in Fig. 5.

For further discussion, only the toplayer compositions of the coatings will be considered. The addition of a second MoS_2 target in favor of a CrAl20 target in the coating process M3 led to a small increase in the Mo and S content in comparison with M2 and M1. The highest Al content of all developed coatings can be proven for the reference (Cr,Al)N. The quantitative values of the chemical composition of the toplayers of the matrix monolayer coatings and the reference coating are shown in Table 4.

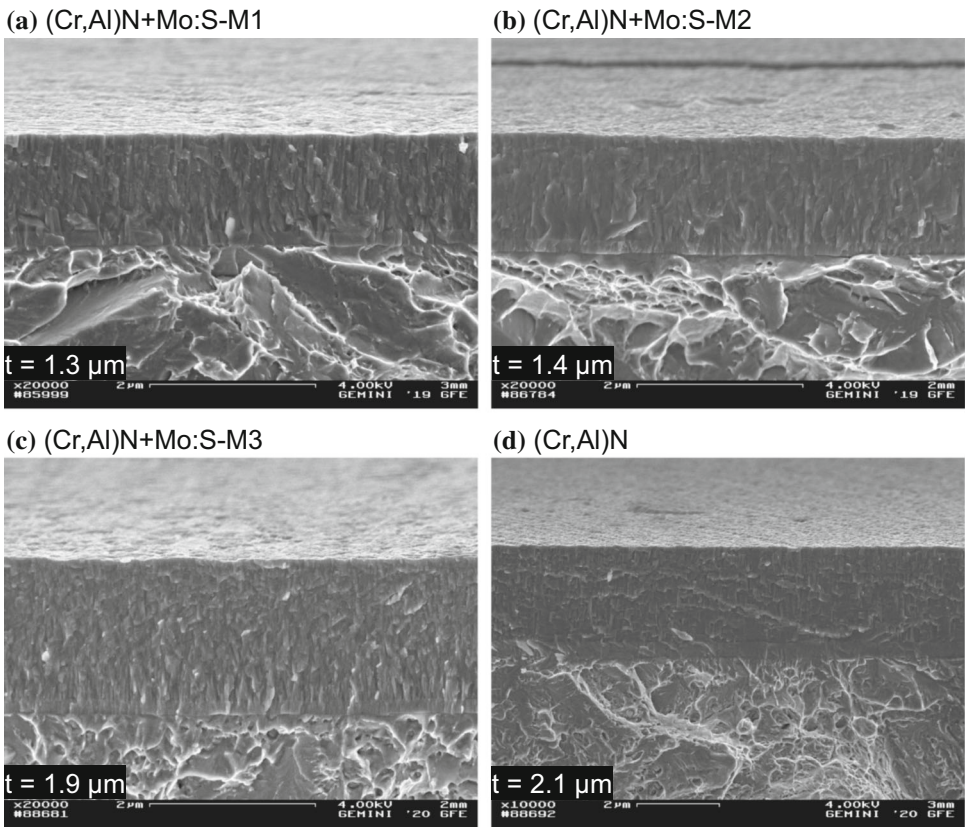

Figure 4 Cross-sectional micrographs of developed (Cr,Al)N+Mo:S matrix coatings and (Cr,Al)N.

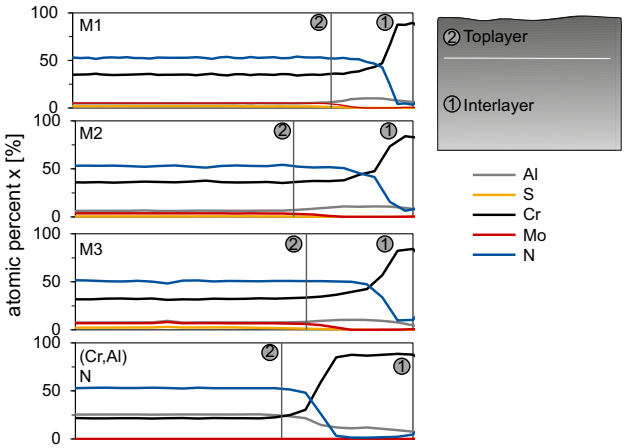

Figure 5 Chemical composition of (Cr,Al)N+Mo:S matrix coatings and (Cr,Al)N by means of EPMA.

Table 4 Quantitative chemical composition of the toplayers of matrix monolayer and (Cr,Al)N reference coating by means of EPMA

Coating/share [at.%]	Cr	Al	N	Mo	S
M1	35.4	4.8	52.8	5.1	1.9
M2	35.3	4.9	52.8	5.1	1.9
M3	31.9	7.5	51.3	6.9	2.4
(Cr,Al)N	21.3	25.9	52.8	–	–

The crystallographic phase analyses of the developed (Cr,Al)N+Mo:S matrix coatings and (Cr,Al)N are presented in the XRD patterns in Fig. 6.

All patterns reveal a cubic CrN phase with corresponding peaks at 2θ ≈ 37.5°, 2θ ≈ 43.6°, 2θ ≈ 63.4° and 2θ ≈ 76.0° and a cubic AlN phase, 2θ ≈ 37.8°, 2θ ≈ 43.9°, 2θ ≈ 63.8° and 2θ ≈ 76.7°. Moreover, a cubic structure was also measured for molybdenum nitride (Mo_2N) phase, 2θ ≈ 37.4°, 2θ ≈ 43.5° and 2θ ≈ 63.1° leading to the conclusion that an additional distortion of the (Cr,Al)N lattice is generated. The peaks of M1 coating appear to be significantly lower in comparison with the M2 und M3 coating, which can be explained through an X-ray amorphous or nanocrystalline structure. The XRD spectra cannot prove the formation of MoS_2. The reason are the low contents of Mo and S for the M1, M2 and M3 coatings. Nevertheless, it can be assumed that Mo and S are incorporated separately in the coating matrix. The crystalline structure of (Cr,Al)N can be proven regarding the cubic CrN and AlN peaks presented in Fig. 6. Furthermore, the indentation hardness H_{IT} and the modulus of indentation E_{IT} of the (Cr,Al)N+Mo:S matrix coatings and the reference coating (Cr,Al)N were determined by nanoindentation, Fig. 7.

The lowest indentation hardness H_{IT} is measured for M1 H_{IT}=(31.0±7.3) GPa in comparison with the two remaining matrix coatings M2 and M3 H_{IT} ≈ (34.0±4.0) GPa. These results are in accordance with the XRD spectra, Fig. 6, showing an increased ratio of crystalline bindings. The indentation hardness H_{IT} and the modulus of indentation E_{IT} of the matrix coatings M2 and M3 do not differ significantly. The highest indentation hardness and modulus of indentation were measured for (Cr,Al)N with H_{IT}=(34.5±5.6) GPa and E_{IT}=(389.0±76.5) GPa. The high deviations from the mean value of indentation hardness and modulus of indentation could not be reduced despite of several measurements. In the next

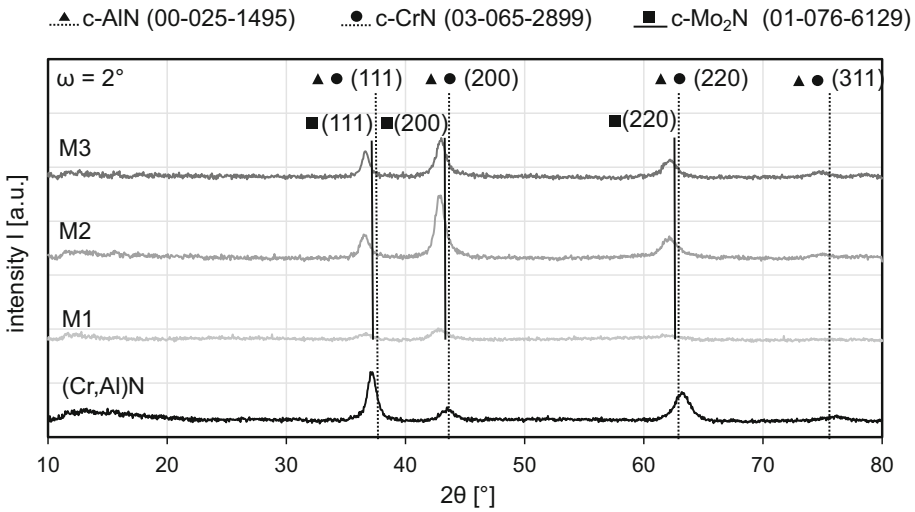

Figure 6 XRD patterns of (Cr,Al)N+Mo:S matrix coatings and (Cr,Al)N.

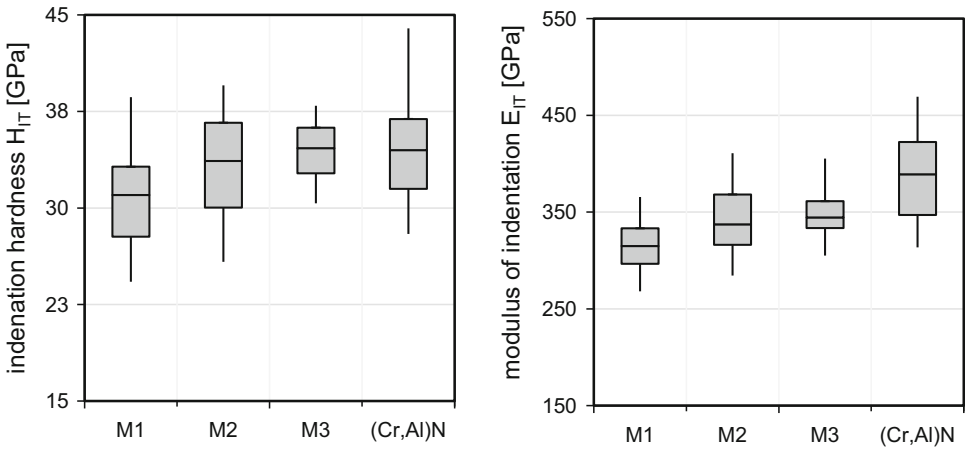

Figure 7 Boxplots of mechanical properties indentation hardness H_{IT} and modulus of indentation E_{IT} (Cr,Al)N+Mo:S matrix coatings and (Cr,Al)N.

step, the compound adhesion between the (Cr,Al)N+Mo:S matrix coatings, (Cr,Al)N and 16MnCr5E was measured by means of scratch test. The critical loads $Lc_{1\text{-}3}$ of the compound M1/16MnCr5E were improved by changing process parameters during the interlayer deposition, Table 2. In [27, 28] it is shown that the parameters HPPMS cathode power, process pressure and bias voltage have an impact on the compound adhesion between coating and substrate material. Hereby, the compound adhesion between matrix coatings and 16MnCr5E could be improved from Lc_3=45 N for M1 to Lc_3=60 N for M2 or M3, Fig. 8. The comparison of the compound systems M2/16MnCr5E and M3/16MnCr5E shows equivalent critical loads but a different plastic deformation behavior. One possible explanation could be the differences in the chemical composition of M2 and M3. The cracks at Lc_3 of M3/16MnCr5E appear to be thinner and narrower and to be less critical than on M2/16MnCr5E. A differing plastic deformation behavior can also be found for the binary system (Cr,Al)N, which shows the highest critical load at Lc_3= 70 N without huge cracks at the edge region of the scratch.

In the next step, tribological analyses were conducted for the matrix coatings, which lead to minimal differences in the CoF, whereby M3 was chosen as representative coating shown in Fig. 9. The decision was based on the comparable coating properties to (Cr,Al)N regarding thickness t, increased Mo content compared to M1 and M2, indentation hardness H_{IT}, modulus of indentation E_{IT} and compound adhesion Lc.

The tribological behavior in a dry-running coating/steel and steel/steel contact was tested at a representative initial Hertzian pressure of p_H= 800 MPa, Fig. 9. In order to analyze the effect of the added Mo and S in the toplayer of the matrix coatings on the CoF, the tribological systems (Cr,Al)N/steel and steel/steel are presented for comparison. The results show a slight friction reduction through the use of (Cr,Al)N+Mo:S regarding the higher CoF of the (Cr,Al)N/steel system. Moreover, the curve progression of the CoF is smooth in comparison with the CoF curve of the steel/steel contact and the (Cr,Al)N/steel contact. However, the CoF of the steel/steel contact still leads to the lowest CoF compared to tribological systems with (Cr,Al)N and (Cr,Al)N+Mo:S. It is believed that the Mo and S ratio in the matrix coating is not high enough for building the required quantity of the solid lubricant MoS_2 in the tribological contact, which would lead to a lowering of the CoF beneath the values of a steel/steel contact. It has to be stated that at this point wear was not analyzed, due to the primary goal of friction reduction in dry-running highly loaded tribological contacts.

Development of a graded (Cr,Al)N+Mo:S coating architecture

Based on the presented results, the coating architecture was varied from a monolayer matrix coating to a graded (Cr,Al)N+Mo:S coating structure. The coating processes were developed based on the promising coating and compound properties of M3/steel. The changes at the toplayer can be found in Table 3. The SEM images of the three graded coatings developed by means of dcMS/HPPMS process are presented in Fig. 10.

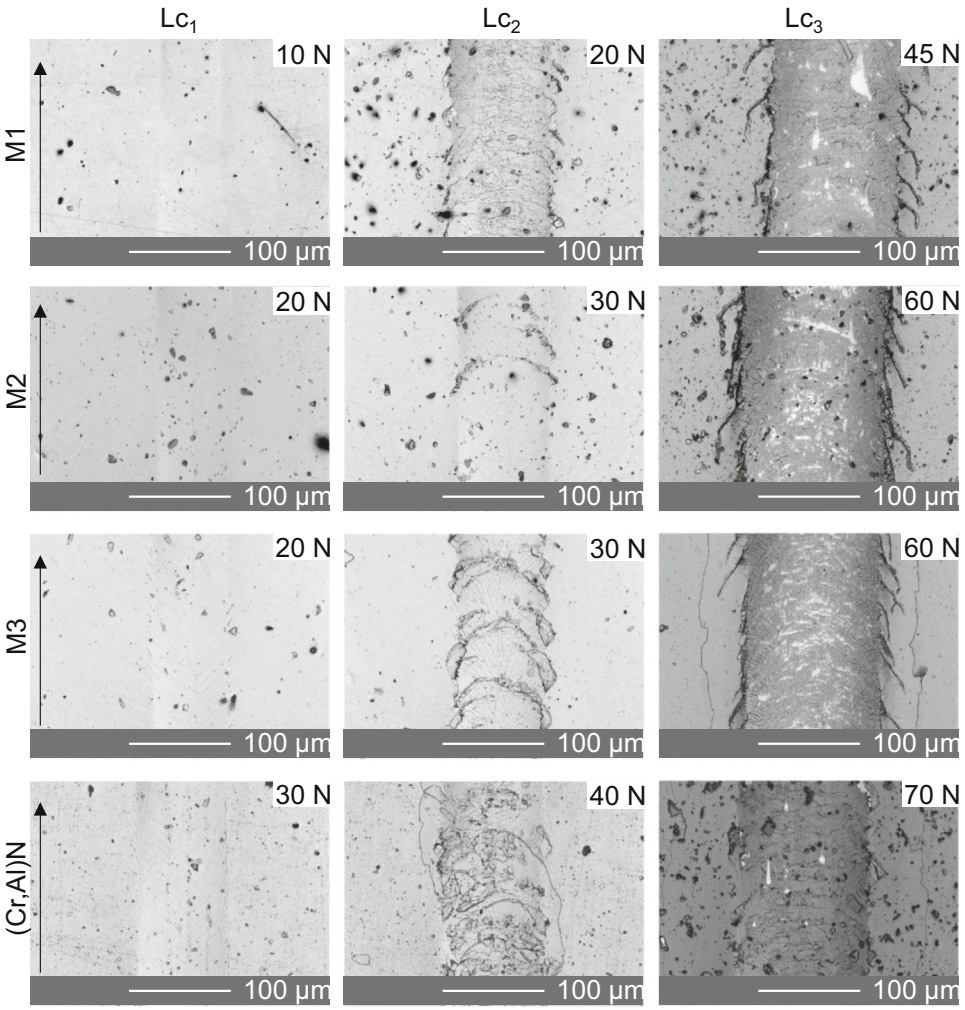

Figure 8 Analysis of compound adhesion between the (Cr,Al)N+Mo:S matrix coatings and (Cr,Al)N on 16MnCr5E by means of scratch test.

The coatings show a columnar morphology and a thickness in a range of 4.0 µm≤t≤5.2 µm. Furthermore, a t=0.8 µm thick amorphous or nanocrystalline toplayer can be seen for the G3 coating. This was achieved by changing the process parameters during the toplayer deposition in comparison with the coating processes G1 und G2, Table 3. In addition, defects on the toplayer topography at G1 and G2 could also be reduced with regard to the coating G3.

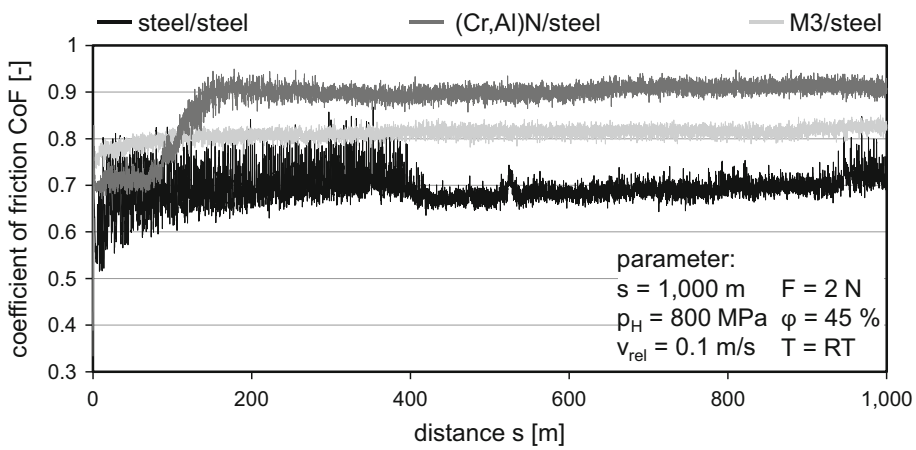

Figure 9 CoF in PoD tests under dry-running conditions for (Cr,Al)N+Mo:S/steel, (Cr,Al)N/steel and steel/steel contact.

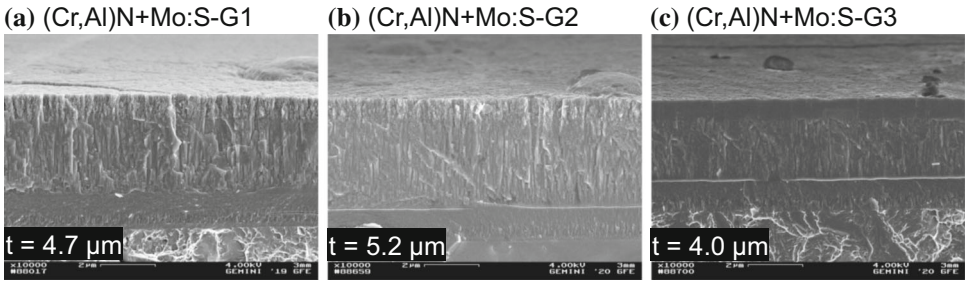

Figure 10 Cross-sectional micrographs of graded (Cr,Al)N+Mo:S coatings.

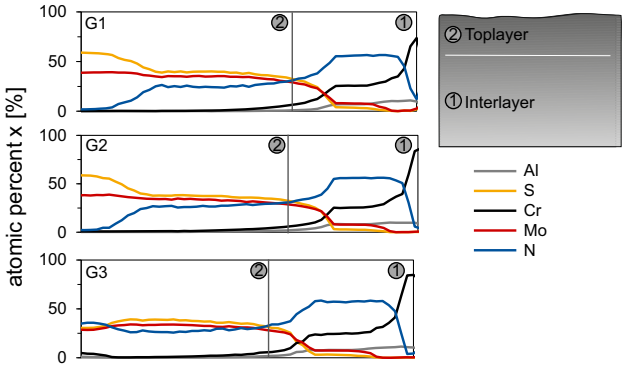

Figure 11 Chemical composition of graded (Cr,Al)N+Mo:S coatings by means of EPMA.

The chemical compositions of the graded coatings are shown in Fig. 11.

Due to changed process parameters compared to the matrix coatings, the Mo and S content is increased within the graded structure. For G2 and G1 an almost stoichiometric ratio of Mo and S can be observed at the toplayer. G3 shows a slight reduction of the Mo and S content in favor of a higher nitrogen, chrome and aluminum content. This is due to an increase in the nitrogen flow and the additional use of the two HPPMS cathodes with CrAl20 targets while the deposition of the toplayer compared to the deposition processes of G1 and G2. The approach was to strengthen the CrAlN nitride matrix in the toplayer, which contains Mo and S. The quantitative values of the chemical composition of the toplayers of the graded (Cr,Al)N+Mo:S coatings are shown in Table 5.

Table 5 Quantitative chemical composition of the toplayers of graded (Cr,Al)N+Mo:S coatings by means of EPMA

Coating/share [at.%]	Cr	Al	N	Mo	S
G1	0.3	0.0	1.7	39.1	58.9
G2	0.9	0.2	1.6	38.4	58.9
G3	5.4	1.2	34.4	28.0	31.0

In Fig. 12, the XRD patterns of the graded (Cr,Al)N+Mo:S coatings are presented to analyze the phase composition. The patterns reveal a hexagonal $Mo_{15}S_{19}$ phase (JCPDS 01-073-5260), $2\theta \approx 11.1$, $2\theta \approx 12.0°$, $2\theta \approx 14.5°$ and $2\theta \approx 33.7°$. In addition, a hexagonal AlN phase (JCPDS 01-073-7288), $2\theta \approx 33.2°$, $2\theta \approx 36.0°$, $2\theta \approx 59.3°$ is found, which results out of the interlayer. According to the observations in the SEM cross-sectional micrographs, crystallographic structure of the graded coating G3 cannot be evaluated by JCPDS cards due to the formation of an amorphous or nanocrystalline toplayer.

It is believed that the exchange of a CrAl20 target to an AlCr30 target as well as the adjustments of process parameters led to the formation of a hexagonal AlN phase, which could favor the formation of hexagonal Mo_aS_b. It is assumed that MoS_2 grows partially epitaxially on the AlN and therefore the hexagonal structure is preferred for G1 and G2. The formation of a cubic phase for CrN and AlN as it was proven for M1–M3 coatings cannot be matched to the coatings G1–G3. Thereby, it has to be taken into account that the XRD spectra are dominated by the structure of the toplayer. The formation of a cubic phase with a transition into a hexagonal phase could be possible at the intermediate layer. This can be concluded because the interlayer coating process part is based on the matrix coating process of M3. In case of G3, further analyses by means of transmission electron microscopy (TEM) have to be conducted, in order to prove, if the MoS_2 toplayer possesses an amorphous or nanocrystalline structure. The evaluation of the indentation hardness and the modulus of indentation of the graded (Cr,Al)N+Mo:S coatings, Fig. 13, shows an increase in the indentation hardness of G1 H_{IT}= (1.4±0.2) GPa to G2 H_{IT}=(2.9±0.2) GPa, which can be related to the exchange of a plugged CrAl20 target to a plugged AlCr30 target.

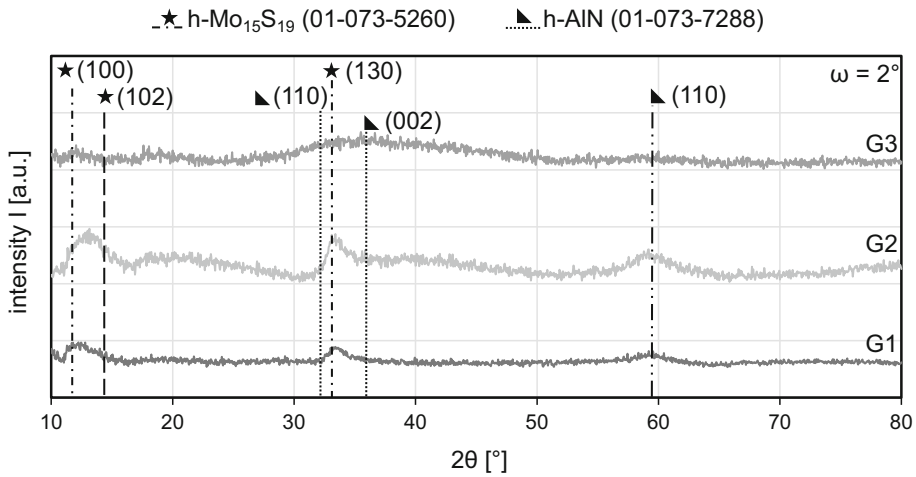

Figure 12 XRD patterns of graded (Cr,Al)N+Mo:S coatings.

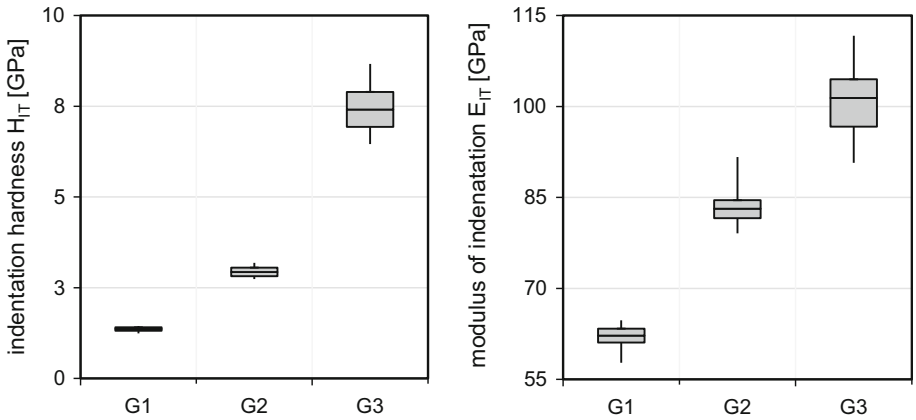

Figure 13 Boxplots of indentation hardness H_{IT} and modulus of indentation E_{IT} of graded (Cr,Al)N+Mo:S coatings.

An explanation could be the slight increase in the alumina content in the coating leading to a higher AlN content. Nevertheless, the measurements are influenced by the soft toplayers of G1–G3 leading to low indentation hardnesses und modulus of indentation. A more significant increase can be measured for the modulus of indentation for G1 at E_{IT}=(62.2±3.6) GPa and G2 at E_{IT}=(83.2±2.5) GPa, which could be related to changes of the target configuration. Further process parameter changes result in an indentation hardness of G3 of H_{IT}=(7.4±1.0) GPa and a modulus of indentation of E_{IT}=(101.4±11.3) GPa. A reason is the changed nitrogen gas flow $Q(N_2)$ and the connected argon pressure p_{Ar} adjustment, Table 3. Furthermore, the Mo:S-containing running-in layer of the coating G3 was stabilized by additional use of the two HPPMS cathodes at the toplayer deposition. Analysis of the compound adhesion between the graded (Cr,Al)N+Mo:S coatings and 16MnCr5E is shown in Fig. 14. The comparison of the critical loads between the coating compounds G1/16MnCr5E, G2/16MnCr5E at Lc_1 ≈ 20 N–30 N and G3/16MnCr5E at Lc_1 ≈ 15 N shows a reduction of the compound adhesion of the latter compound. An explanation cannot be given yet.

In sum, the coating delamination caused by the scratch tip appears to be lowered for the compound G3/16MnCr5E compared to the remaining two developed graded coating/steel compounds, due to less delamination at the edge region of the scratch. Even though the compound G3/16MnCr5E shows low values for Lc_1, the maximum critical load Lc_3 is in the same order as for the compounds G1/16MnCr5E and G2/16MnCr5E. Due to the promising results of M3 and G3 and the reference (Cr,Al)N, these coatings were chosen for tribological analysis at p_H=400 MPa, p_H=600 MPa, p_H=800 MPa and p_H=1300 MPa under dry-running in a coating/steel contact compared with a steel/steel contact.

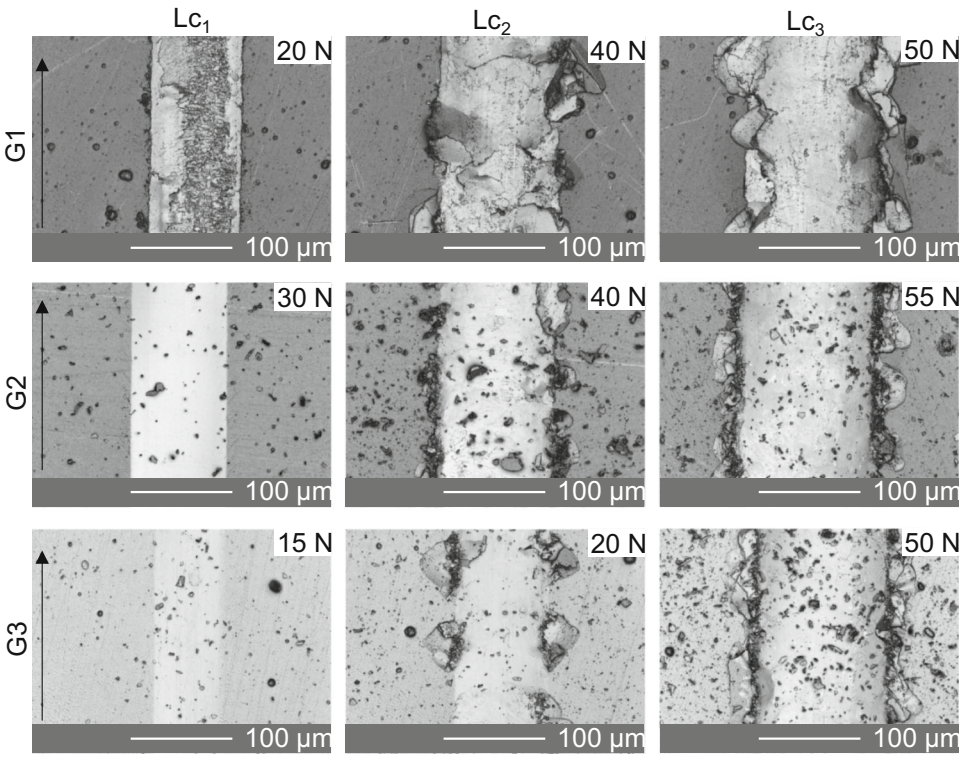

Figure 14 Analysis of compound adhesion between the graded (Cr,Al)N+Mo:S coatings and 16MnCr5E by means of scratch test.

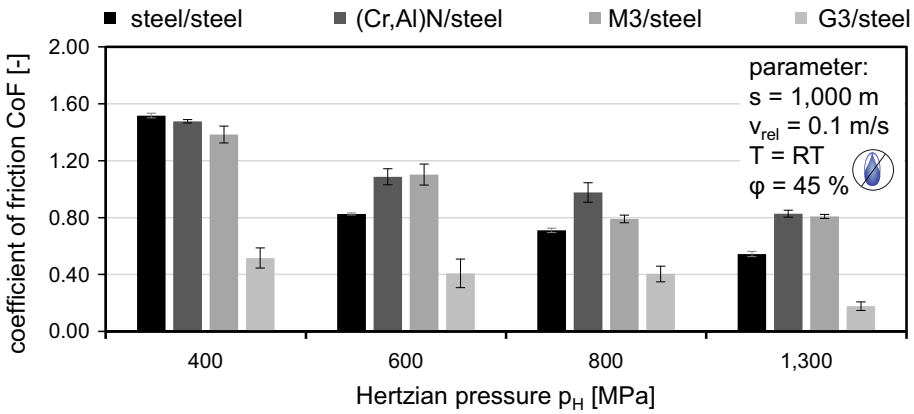

Figure 15 Average CoF obtained from two PoD tests under dry-running conditions at different loads p_H of the final s=500 m running distance.

Tribological analysis

Figure 15 shows the mean values of the CoF as a function of the initial Hertzian pressures for four different contacts under dry-running conditions. It can be seen that the CoF is reduced by increasing the Hertzian pressure from p_H=400 to p_H=1300 MPa.

An explanation regarding the steel/steel contacts can be given through the possible increased formation of friction reducing iron oxides like Fe_3O_4 as proposed in [29] which is also discussed in the model of Quinn [30]. At an initial Hertzian pressure of p_H= 400 MPa and p_H=600 MPa, the CoF of the systems (Cr,Al)N/steel and M3/steel is situated in the same area. With regard to the higher initial Hertzian pressures at p_H=800 MPa and p_H=1300 MPa, the CoF of the tribological system M3/steel does not show a significant difference to the CoF of (Cr,Al)N/steel. However, in case of M3/steel a formation of the solid lubricant MoS_2 during the tribological contact due to higher flash temperatures and wear is possible. Thereby, an opening of the Mo and S reservoirs at the toplayer of the coating is enabled. The lowest CoF was measured by the use of G3 for all considered tribological loads.

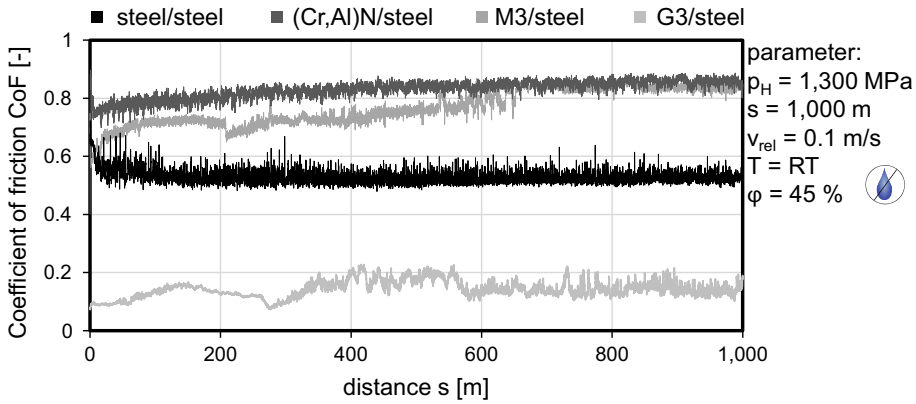

Figure 16 PoD tests under dry-running conditions at an initial Hertzian pressure p_H= 1300 MPa.

In addition, the CoF further reduced from 0.52≤ CoF≤0.18 by increasing load conditions, leading to the possible conclusion that more MoS_2 is built in the tribological G3/steel contact. Moreover, the additional formation of Mo_xO_y in the tribofilm is possible. The differences between the four considered contacts steel/steel, (Cr,Al)N/steel, M3/steel and G3/steel can also be observed in the curve progressions as shown in Fig. 16. Herein, the results are exemplarily shown for an initial Hertzian pressure p_H=1300 MPa. With regard to the curves of the contacts between (Cr,Al)N/steel, M3/steel it can be observed that the small shares of Mo ≈ 7 at.% and S ≈ 3 at.% at the toplayer of M3 has no friction reducing effect. The measured CoF for a steel/steel contact is significantly lower compared to the use of (Cr,Al)N and M3, which can be a result of formed oxides as explained above. A stable curve progression at a low CoF value was measured for the G3/steel contact.

The shares of Mo ≈ 28 at.% and S ≈ 31 at.% at the toplayer of G3 appears to be the decisive factor in case of friction reduction. In addition, a stable curve progression can be observed as well. After tribological testing, the 100Cr6 counterparts as well as the wear tracks were analyzed by means of CLSM, Fig. 17. All counterparts show abrasive wear scars regarding the grooves on the topography, Fig. 17b. A difference can be observed in the diameter of the wear areas of the counterparts, which is increased in the steel/steel contact as well as for the (Cr,Al)N/

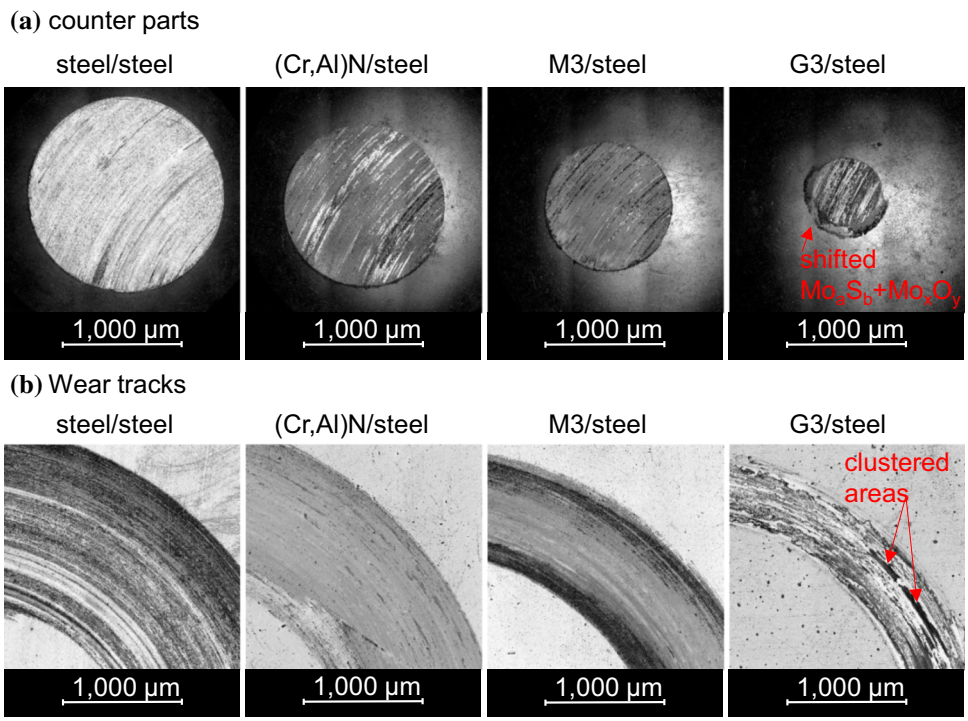

Figure 17 (a) Wear area at the 100Cr6 counterparts and (b) wear track on steel and on coated samples under Hertzian pressure p_H=1300 MPa.

steel and M3/steel contact compared to the wear area of the counterpart in the G3/steel contact, Fig. 17a. Herein, the deposition of a thick layer at the edge region of the circle area for the tribological system G3/steel can be observed. It is assumed that a Mo_a-S_b+Mo_xO_y layer is formed during the tribological contact, which is then transferred from the G3 coating to the counterpart, Fig. 17a.

In comparison of the width of the wear tracks, Fig. 17b, a reduction for the Mo- and S-containing coatings can be seen. All tracks show abrasive wear marks, which correspond to the grooves on the counterparts. With regard to the wear track of the steel/steel contact, adhesive wear scars cannot be excluded. Moreover, the topography of the wear track on G3 shows black clustered areas, which are not identified to be a result of adhesive wear. Indeed due to the low friction results, the images of the counterparts and the presence of MoS_2 in the toplayer of the as-deposited coatings, it is believed that MoS_2 is transferred in the grooves of the wear track. Furthermore, the formation of Mo_xO_y is possible due to the presence of oxygen in the fluid-free tribological contact. Figure 18 presents the wear volume of the counterparts W_{VCP} in dependence of different loading conditions. In contrast to the CoF, wear is increased by rising Hertzian pressure from p_H=400 to p_H=1300 MPa, which can be explained by an enlargement of abrasive wear in the steel/steel contact. Due to the increasing initial Hertzian load, a local micro-welding might occur more frequently leading to adhesive wear at the 100Cr6 ball in steel/steel contacts. A significant wear reduction was measured for the tribological contact with the (Cr,Al)N or matrix coating in comparison with the steel/steel contact, Fig. 18.

As a result of the addition of Mo and S at the toplayer of M3 in contrast to (Cr,Al)N, a further reduction of the wear of the counterpart is measured. With regard to the small differences between (Cr,Al)N/steel and M3/steel regarding the CoF, the wear reduction cannot be explained by the formation of MoS_2 but probably due to formation of molybdenum oxide Mo_xO_y as in [31]. In case of the graded (Cr,Al)N+Mo:S coating, the wear of the counterparts appears to be the lowest, which can be attributed to the possible transfer of MoS_2 as well as the formation of Mo_xO_y. The wear volume of the wear tracks after tribological testing is shown in Fig. 19. The highest wear volume can be observed for steel/steel contacts for all considered Hertzian pressures p_H. A significant reduction of wear volume from p_H=600 MPa to p_H=800 MPa can be observed.

Here, it is possible that at p_H=800 MPa, the tribological steel/steel system enables the formation of a Fe_cO_d/Cr_eO_f tribofilm, which works in an ideal state. It is assumed that in this ideal state the tribological parameters lead to a continuous formation and wear of the oxidic tribofilm in a balanced ratio. At higher or lower Hertzian pressures, this equilibrium shifts to the disadvantage between the formation of a protective oxidic tribofilm and wear. Moreover, the wear of the (Cr,Al)N and M3 coated samples was not measurable on the samples due to neglectable changes irrespective of the mechanical loads. In contrast thereto, the wear volume of the G3 coated basic parts

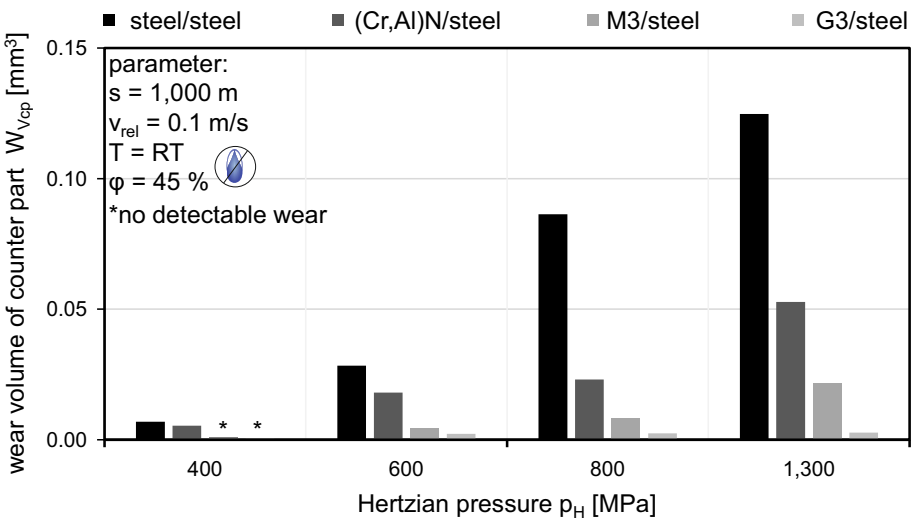

Figure 18 Wear volume of 100Cr6 counterparts after dry-running conditions under different loads p_H.

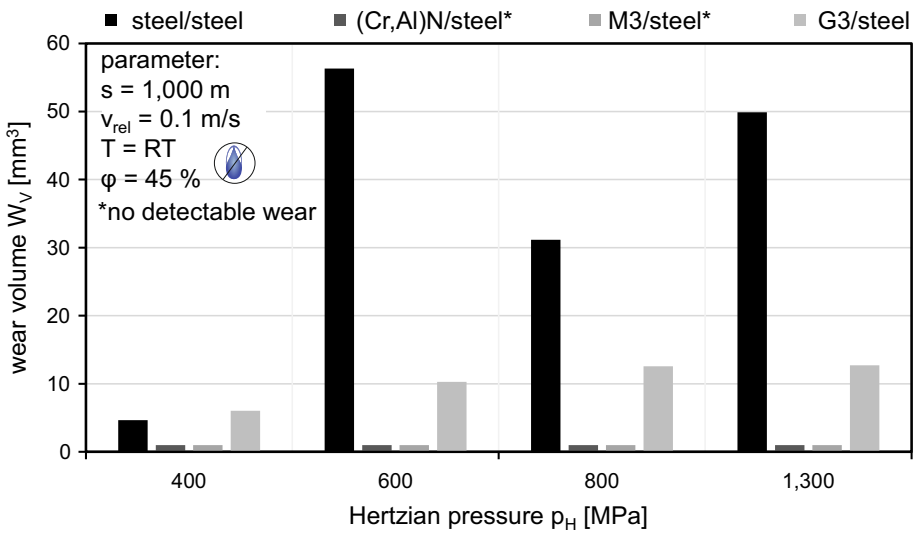

Figure 19 Wear volume of wear tracks after dry-running conditions under different loads p_H.

slightly increases from p_H=400 to p_H=1300 MPa. Nevertheless, the wear volume of G3 increases from p_H=400 MPa till p_H=800 MPa but stays at the same level even at a higher load of p_H=1300 MPa. Furthermore, the wear volume is significantly reduced in comparison with the basic parts in the steel/steel contacts. The results prove again that hardness and wear resistance are not in any linear relationship to each other regarding the presented mechanical properties of M3 and G3 coating in correlation with the wear reduction. Therefore, also the chemical composition and the formation of tribo-induced layers have to be taken into account.

Chemical analysis of the wear tack by Raman spectroscopy

Finally, G3 and 100Cr6 were chosen for chemical analysis by Raman spectroscopy due to the low CoF and wear of the counterpart during tribological testing. The wear track of a G3 basic part and a 100Cr6 counterpart after tribological testing at p_H=400 MPa, T=20 °C, s=1000 m and v=0.1 m/s were exemplarily analyzed, Figs. 20a and 21a. In addition, a reference spectrum was recorded in each case, Figs. 20b and 21b. Due to curve fittings of the Raman spectra, the positions of the individual peaks could be identified as shown in Figs. 20, 21, Tables 6, 7 and 8.

The chemical analysis of the as-deposited G3 basic part shows the formation of MoO_2 and MoO_3, Table 6, which can be a result of the laser power applied on the surface. This leads to the assumption that molybdenum is available in an unbounded metallic form at the toplayer of G3. The peaks at $\tilde{\upsilon}$= 361 cm^{-1} and $\tilde{\upsilon}$=407 cm^{-1} can be assigned to MoS_2.

The first peak of MoS_2 appears to be hidden beneath the MoO_2 peak at $\tilde{\upsilon}$=335 cm^{-1}. Moreover, amorphous carbon was proven on the as-deposited surface, which can be a result of an alcohol cleaning or a contamination during the handling of the samples. The analysis inside the wear track proves the formation of iron oxide like hematite α-Fe_2O_3, magnetite Fe_3O_4, maghemite γ-Fe_2O_3 as well as molybdenum oxides MoO_2, MoO_3, Mo_xO_y and MoS_2. The appearance of amorphous carbon in the wear track was predominantly excluded due to the high shares of iron in contrast to carbon of the uncoated 100Cr6 counterpart. However, the assignment for the peak was listed in the area of 1100 $cm^{-1} \leq \tilde{\upsilon} \leq 1600$ cm^{-1}. Based on the intensities in the Raman spectra, the shares of molybdenum oxides is significantly higher in comparison with MoS_2, leading to the assumption that the friction and wear reduction is mainly determined by the formation of the molybdenum oxides. The iron oxides are a result of the abrasion of the 100Cr6 counterpart. Due to the low shares of iron oxides within the Raman spectra, it is assumed that they have a subordinated effect on friction and wear.

Based on these results, a 100Cr6 counterpart was analyzed to get an impression of the transfer layer during the tribological contact, Fig. 21. The detection of Cr_2O_3 is in accordance with the 100Cr6 surface after tribological testing. In addition, one peak was assigned to magnetite Fe_3O_4, which is a result of the oxidation of the 100Cr6 surface. Furthermore, the Raman spectra prove the formation of MoS_2, MoO_3

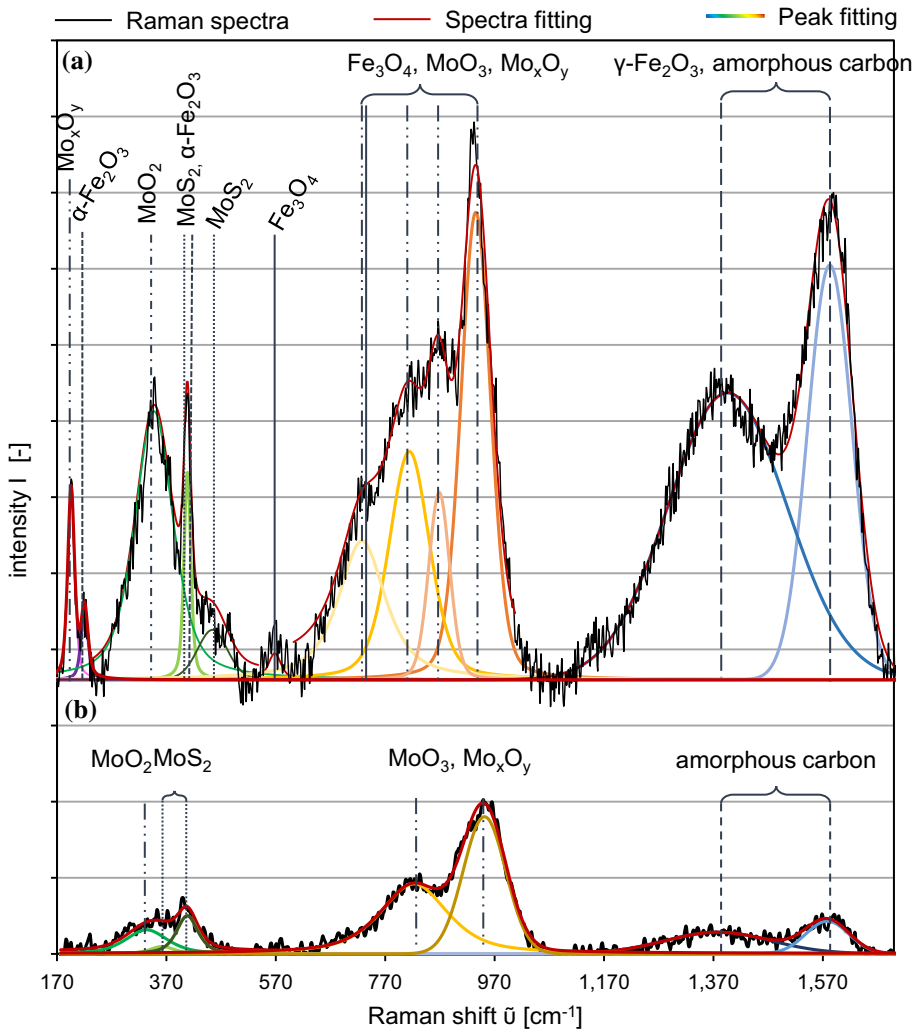

Figure 20 Raman spectra of (a) G3 inside the wear track after tribological testing at p_H =400 MPa, T=20 °C, s= 1000 m, v=0.1 m/s and (b)as-deposited.

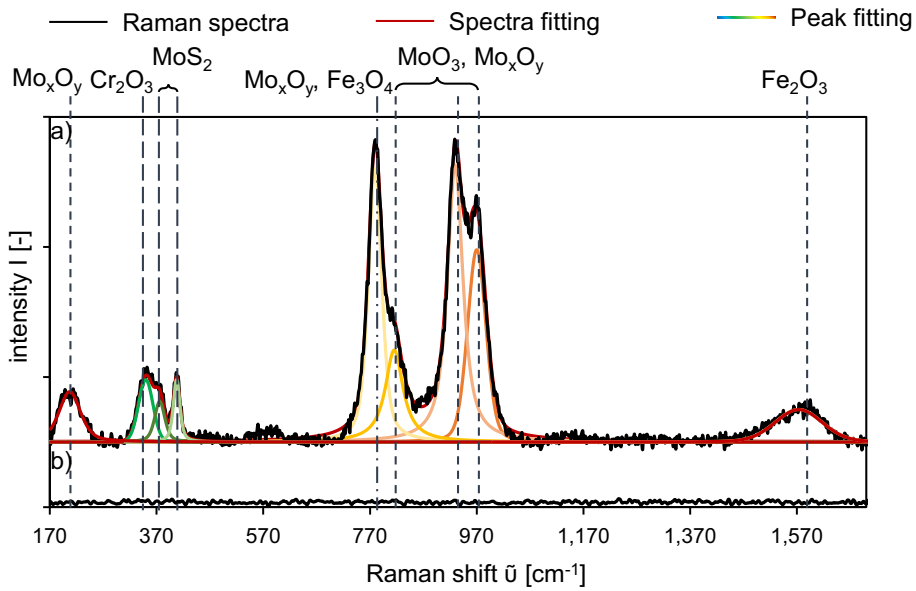

Figure 21 Raman spectra of (a) 100Cr6 counterpart after tribological testing at p_H= 400 MPa, T=20 °C, s= 1000 m, v=0.1 m/s and (b) 100Cr6 untested.

Table 6 Overview of the assignment of measured Raman peaks at base part as deposited

Binding	Measured peak position at reference	Literature	Source
MoO_2	335	340	[32]
MoS_2	361	375	[33]
MoS_2	408	400	[33]
MoO_3, Mo_xO_y	820	820, 818	[33, 34]
MoO_3	950	952	[34]
Amorphous carbon	1380	1360	[35]
Amorphous carbon	1580	1560	[35]

Table 7 Overview of the assignment of measured Raman peaks at base part after tribological testing

Binding	Measured peak position inside wear track	Literature	Source
Mo_xO_y	196	198	[34]
α-Fe_2O_3	220	226	[36]
MoO_2	347	347	[32]
MoS_2, α-Fe_2O_3	410	400	[33, 37]
MoS_2	452	450	[38]
Fe_3O_4	568	560	[39]
Mo_xO_y, Fe_3O_4	727	744, 750	[34, 40]
MoO_3, Mo_xO_y	815	820, 818	[33, 34]
MoO_3, Mo_xO_y	867	843	[32]
Mo_xO_y	935	922	[34]
γ-Fe_2O_3	1395	1400	[41]
γ-Fe_2O_3	1585	1580	[41]

Table 8 Overview of the assignment of measured Raman peaks at 100Cr6 counterpart after tribological testing

Binding	Measured peak position	Literature	Source
Mo_xO_y	207	198	[34]
Cr_2O_3	350	348	[42]
MoS_2	377	375	[33]
MoS_2	407	400	[33]
Mo_xO_y, Fe_3O_4	778	744, 750	[34, 40]
MoO_3, Mo_xO_y	814	820, 818	[33, 34]
Mo_xO_y	929	922	[34]
MoO_3, Mo_xO_y	970	995, 990	[33, 34]
γ-Fe_2O_3	1572	1580	[41]

and Mo_xO_y and transfer of the tribofilm from the basic part to the 100Cr6 counterpart during the tribological contact, Table 8.

Due to the tribofilm transfer from the basic part to the counterpart, a friction reduction can be observed in the tribological analysis. The analysis of the untested 100Cr6 counterpart proves that the formation of iron oxides is a result of the tribological contact.

In order to prove the exact chemical composition, further chemical analysis by Raman spectroscopy and X-ray photoelectron spectroscopy (XPS) will be needed. Based on these results and further optical spectrometry, an analysis of the supply mechanism of the graded (Cr,Al)N+Mo:S coating and the transfer mechanism of the tribofilm is possible. Here, a deeper understanding of the tribological contact can be achieved.

Summary and conclusion

In this study the process and material development of self-lubricating triboactive (Cr,Al)N+Mo:S coatings for fluid-free applications were shown. Matrix

and graded coating architectures were analyzed regarding morphology, chemical composition, crystallographic structure and indentation hardness and modulus of indentation as well as the compound adhesion between coating and steel. In the next step, tribological tests at different loads ranging from an initial Hertzian pressure p_H=400 MPa to p_H= 1300 MPa were conducted. The key results can be summarized as follows:

- Development of low temperature $T \leq 300$ °C monolayer matrix and graded (Cr,Al)N+Mo:S coating processes by means of dcMS/HPPMS on 16MnCr5E
- Incorporation of different Mo:S ratios in different coating architectures in a matrix monolayer and a graded coating
- Mo- and S-rich toplayer of graded (Cr,Al)N+Mo:S coatings
- MoS_2-, MoO_3-, MoO_2- and Mo_xO_y-containing tribofilm proves the supply mechanism of the (Cr,Al)N+Mo:S coating and transfer mechanism of tribofilm on uncoated 100Cr6 counterpart
- Regardless of the low indentation hardness and the low modulus of indentation of the graded (Cr,Al)N+Mo:S coating in comparison with matrix (Cr,Al)N+Mo:S, a significant reduction in friction and wear was achieved

In the next step, chemical analyses by means of Raman spectroscopy on the wear tracks and on the counterparts will be proceeded to get a deeper view on the supply mechanism of self-lubricating triboactive (Cr,Al)N+Mo:S coatings. The results can be supported by SEM analyses of the wear tracks and counterparts of coated and uncoated samples after tribological testing. Furthermore, photoemission spectroscopy (XPS) can help to prove the results by Raman spectroscopy and reveal the binding character of the tribo-induced layers.

Acknowledgements

The authors gratefully acknowledge the financial support of the German Research Foundation, Deutsche Forschungsgemeinschaft (DFG), within the project "Dry Lubrication of Spur Gears—Tribological Analysis and Constructive Design" BO 1979/66-1.

Funding

Open Access funding enabled and organized by Projekt DEAL. This study was funded by German Research Foundation, Deutsche Forschungsgemeinschaft (DFG), within the project "Dry Lubrication of Spur Gears—Tribological Analysis and Constructive Design" BO 1979/66-1.

Declarations

Conflict of interest The authors declare that they have no known competing financial interests or personal relationships that could have appeared to influence the work reported in this paper.

References

[1] Birkhofer H, Kümmerle T (2012) Feststoffgeschmierte Wälzlager: Einsatz, Grundlagen und Auslegung. VDI-Buch. Springer, Berlin, Heidelberg

[2] Martens S (2008) Ölfreie Industriegetriebe: Maßnahmen und Möglichkeiten zur Minimierung bzw. Eliminierung herkömmlicher Schmierstoffe. Dissertation, Dresden, p 223. https://katalog.slub-dresden.de/id/0-1374188077

[3] Schlecht B, Martens S, Röhmhild I (2005) Approaches to oil-free gears, VDI Berichte 1904 II, 1904 II, p 1021–1034. https://www.scopus.com/record/display.uri?eid=2-s2.0-27344460430&origin=AuthorNamesList&txGid=7c8652c9ba7321b7eb8755369416d587

[4] Röhmhild I (1998) Getriebe ohne Öl, Getriebe geringer Verluste: Forschungsbericht Deutsche Bundesstiftung

Umwelt, Forschungsbericht Deutsche Bundesstiftung Umwelt, Vol 1, p 164

[5] Singer IL, Fayeulle S, Ehni PD (1996) Wear behavior of triode-sputtered MoS_2 coatings in dry sliding contact with steel and ceramics. Wear. https://doi.org/10.1016/0043-1648(95)06661-6

[6] Stupp BC (1981) Synergistic effects of metals co-sputtered with MoS_2. Thin Solid Films. https://doi.org/10.1016/0040-6090(81)90023-7

[7] Teer DG, Hampshire J, Fox V, Bellido-Gonzalez V (1997) The tribological properties of MoS_2/metal composite coatings deposited by closed field magnetron sputtering. Surf Coat Technol. https://doi.org/10.1016/S0257-8972(97)00498-2

[8] Ma KJ, Chao CL, Liu DS, Chen YT, Shieh MB (2002) Friction and wear behaviour of TiN/Au, TiN/MoS_2 and TiN/TiCN/a-C: H coatings. J Mater Process Technol. https://doi.org/10.1016/S0924-0136(02)00123-1

[9] Bobzin K (2017) High-performance coatings for cutting tools. CIRP J Manuf Sci Technol. https://doi.org/10.1016/j.cirpj.2016.11.004

[10] Buhl R, Pulker HK, Moll E (1981) TiN coatings on steel. Thin Solid Films. https://doi.org/10.1016/0040-6090(81)90233-9

[11] Knotek O, Löffler F, Scholl H-J (1991) Properties of arc-evaporated CrN and (Cr, Al)N coatings. Surf Coat Technol. https://doi.org/10.1016/0257-8972(91)90205-B

[12] Leyendecker T, Lemmer O, Esser S, Ebberink J (1991) The development of the PVD coating TiAlN as a commercial coating for cutting tools. Surf Coat Technol. https://doi.org/10.1016/0257-8972(91)90142-J

[13] Huang ZP, Sun Y, Bell T (1994) Friction behaviour of TiN, CrN and (TiAl)N coatings. Wear. https://doi.org/10.1016/0043-1648(94)90252-6

[14] Bobzin K, Brögelmann T, Kruppe NC, Hoffmann DC, Klocke F, Mattfeld P, Trauth D, Hild R (2018) Tribological studies on self-lubricating (Cr, Al)N+Mo: S coatings at elevated temperature. Surf Coat Technol. https://doi.org/10.1016/j.surfcoat.2018.06.067

[15] Kim SK, Cha BC (2004) Deposition of CrN–MoS_2 thin films by DC magnetron sputtering. Surf Coat Technol. https://doi.org/10.1016/j.surfcoat.2004.08.013

[16] Gilmore R, Baker MA, Gibson PN, Gissler W, Stoiber M, Losbichler P, Mitterer C (1998) Low-friction TiN–MoS_2 coatings produced by dc magnetron co-deposition. Surf Coat Technol. https://doi.org/10.1016/S0257-8972(98)00602-1

[17] Bobzin K, Brögelmann T, Kalscheuer C, Naderi M (2016) Hybrid dcMS/HPPMS PVD nitride and oxynitride hard coatings for adhesion and abrasion reduction in plastics processing. Surf Coat Technol. https://doi.org/10.1016/j.surfcoat.2016.07.103

[18] Ehiasarian AP, Wen JG, Petrov I (2007) Interface microstructure engineering by high power impulse magnetron sputtering for the enhancement of adhesion. J Appl Phys. https://doi.org/10.1063/1.2697052

[19] Tian X, Ma Y, Hu J, Bi M, Gong C, Chu PK (2017) Microstructure and mechanical properties of $(AlTi)_x N_{1-x}$ films by magnetic-field-enhanced high power impulse magnetron sputtering. J Vac Sci Technol A Vac Surf Films. https://doi.org/10.1116/1.4971202

[20] Paulitsch J, Schenkel M, Schintlmeister A, Hutter H, Mayrhofer PH (2010) Low friction CrN/TiN multilayer coatings prepared by a hybrid high power impulse magnetron sputtering/DC magnetron sputtering deposition technique. Thin Solid Films. https://doi.org/10.1016/j.tsf.2010.05.061

[21] Bobzin K, Bagcivan N, Ewering M, Brugnara RH, Theiß S (2011) DC-MSIP/HPPMS (Cr, Al, V)N and (Cr, Al, W)N thin films for high-temperature friction reduction. Surf Coat Technol. https://doi.org/10.1016/j.surfcoat.2010.10.056

[22] Bobzin K, Brögelmann T, Kalscheuer C (2017) Triboactive CrAlN+X hybrid dcMS/HPPMS PVD nitride hard coatings for friction and wear reduction on components. Surf Coat Technol. https://doi.org/10.1016/j.surfcoat.2017.06.089

[23] Bobzin K, Brögelmann T, Kruppe NC (2018) Enhanced PVD process control by online substrate temperature measurement. Surf Coat Technol. https://doi.org/10.1016/j.surfcoat.2018.07.096

[24] Oliver WC, Pharr GM (1992) An improved technique for determining hardness and elastic modulus using load and displacement sensing indentation experiments. J Mater Res. https://doi.org/10.1557/JMR.1992.1564

[25] DIN EN ISO 20502:2016-11, Hochleistungskeramik-Bestimmung der Haftung von keramischen Schichten mit dem Ritztest (ISO 20502:2005 einschließlich Cor 1:2009); Deutsche Fassung EN ISO 20502:2016, Berlin. Beuth Verlag GmbH, p 38

[26] Data sheet 16MnCr5E Stauberstahl, p 1. https://www.stauberstahl.com/fileadmin/Werkstoff-PDF/Werkstoff-17131-Datenblatt.pdf. Accessed 19 Feb 2021

[27] Bobzin K, Brögelmann T, Kruppe NC, Engels M (2018) Investigations on the substrate bias influence on reactive HPPMS plasmas. Thin Solid Films. https://doi.org/10.1016/j.tsf.2018.07.048

[28] Broitman E, Hultman L (2012) Adhesion improvement of carbon-based coatings through a high ionization deposition technique. J Phys Conf Ser. https://doi.org/10.1088/1742-6596/370/1/012009

[29] Kong H, Yoon E-S, Kwon OK (1995) Self-formation of protective oxide films at dry sliding mild steel surfaces under a medium vacuum. Wear. https://doi.org/10.1016/0043-1648(95)90039-X

[30] Quinn TFJ, Rowson DM, Sullivan JL (1980) Application of the oxidational theory of mild wear to the sliding wear of low alloy steel. Wear. https://doi.org/10.1016/0043-1648(80)90002-2

[31] Suszko T, Gulbiński W, Jagielski J (2005) The role of surface oxidation in friction processes on molybdenum nitride thin films. Surf Coat Technol. https://doi.org/10.1016/j.surfcoat.2004.07.119

[32] Dieterle M, Mestl G (2002) Raman spectroscopy of molybdenum oxides. Phys Chem Chem Phys. https://doi.org/10.1039/B107046K

[33] Windom BC, Sawyer WG, Hahn DW (2011) A Raman spectroscopic study of MoS_2 and MoO_3: applications to tribological systems. Tribol Lett. https://doi.org/10.1007/s11249-011-9774-x

[34] Seguin L, Figlarz M, Cavagnat R, Lassègues J-C (1995) Infrared and Raman spectra of MoO3 molybdenum trioxides and $MoO_3{\cdot}xH_2O$ molybdenum trioxide hydrates. Spectrochimica Acta Part A Mol Biomol Spectrosc. https://doi.org/10.1016/0584-8539(94)00247-9

[35] Casiraghi C, Ferrari AC, Robertson J (2005) Raman spectroscopy of hydrogenated amorphous carbons. Phys Rev B. https://doi.org/10.1103/PhysRevB.72.085401

[36] Beattie IR, Gilson TR (1970) The single-crystal Raman spectra of nearly opaque materials. Iron(III) oxide and chromium(III) oxide. J Chem Soc A. https://doi.org/10.1039/J19700000980

[37] de Faria DLA, Venâncio Silva S, de Oliveira MT (1997) Raman microspectroscopy of some iron oxides and oxyhydroxides. J Raman Spectrosc. https://doi.org/10.1002/(SICI)1097-4555(199711)28:11%3c873:AID-JRS177%3e3.0.CO;2-B

[38] Chen JM, Wang CS (1974) Second order Raman spectrum of MoS_2. Solid State Commun. https://doi.org/10.1016/0038-1098(74)90150-1

[39] Wieting TJ, Verble JL (1971) Infrared and Raman studies of long-wavelength optical phonons in hexagonal MoS_2. Phys Rev B. https://doi.org/10.1103/PhysRevB.3.4286

[40] Shebanova ON, Lazor P (2003) Raman study of magnetite (Fe_3O_4): laser-induced thermal effects and oxidation. J Raman Spectrosc. https://doi.org/10.1002/jrs.1056

[41] Mazzetti L, Thistlethwaite PJ (2002) Raman spectra and thermal transformations of ferrihydrite and schwertmannite. J Raman Spectrosc. https://doi.org/10.1002/jrs.830

[42] Barshilia HC, Selvakumar N, Deepthi B, Rajam KS (2006) A comparative study of reactive direct current magnetron sputtered CrAlN and CrN coatings. Surf Coat Technol. https://doi.org/10.1016/j.surfcoat.2006.03.037